Controllable Template-Assisted Electrodeposition of Single- and Multi-Walled Nanotube Arrays for Electrochemical Energy Storage

Zi-Long Wang, Rui Guo, Liang-Xin Ding, Ye-Xiang Tong & Gao-Ren Li

MOE Laboratory of Bioinorganic and Synthetic Chemistry, KLGHEI of Environment and Energy Chemistry, School of Chemistry and Chemical Engineering, Sun Yat-sen University, Guangzhou 510275, P. R. China.

Here we explored a novel ZnO nanorod array template-assisted electrodeposition route to synthesize large-scale single-walled polypyrrole (PPy) nanotube arrays (NTAs) and multi-walled MnO_2/PPy/MnO_2 NTAs. The structures of nanotubes, such as external and inner diameters, wall thicknesses, and lengths, can be well controlled by adjusting the diameters and lengths of ZnO nanorods and deposition time. The synthesized hybrid MnO_2/PPy/MnO_2 triple-walled nanotube arrays (TNTAs) as electrodes showed high supercapacitive perporties, excellent long-term cycling stability, and high energy and power densities. The PPy layers in MnO_2/PPy/MnO_2 TNTAs provide reliable electrical connections to MnO_2 shells and uniquely serve as highly conductive cores to support the redox reactions in the active two-double MnO_2 shells with highly electrolytic accessible surface area. The fabricated multi-walled NTAs allow high efficient utilization of electrode materials with facilitated transports of ions and electrons. The outstanding performance makes MnO_2/PPy/MnO_2 TNTAs promising candidates for supercapacitor electrodes.

Hollow nanotubes are attracting a great deal of attention because of their fundamental significance and potential applications in electric devices, sensors, and catalysis[1–5]. Various methods have been developed for the synthesis of nanotubes, such as high temperature evaporation[6], colloidal growth[7], hydrothermal synthesis[8,9], anodic oxidation[10–12], and template- and surfactant-assisted growth tech-niques[13–24]. Recently, there is increasing interest in the template-assisted method because it has been used to synthesize various nanotubes composed of many types of materials, such as silica[25,26], metal oxides[27–29], polymers[30,31], and biological macro-molecules[32]. An important characteristic of template synthesis method is the ability to control the dimensions of nanotubes obtained[33]. For example, the outside diameters of nanotubes can be well determined by the diameters of pores in template, and the lengths can be well determined by the thickness of template.

However, up to now, the template-assisted method is still difficult to control the inside diameters of nano-tubes[34–37]. For some applications, precisely controlling the inside diameters is absolutely essential[38]. It is also highly difficult to realize the design and synthesis of multi-walled nanotubes by the template-assisted method. Recently, the multi-walled nanotubes have attracted much interest because of their special properties[39–41]. Based on the above considerations, here we set up a novel ZnO nanorod array template-assisted electrodeposition method for the design and synthesis of single- and multi-walled nanotube arrays (NTAs) because this method enables excellent control of NTAs. Here single-walled polypyrrole (PPy) NTAs and triple-walled MnO_2/PPy/MnO_2 NTAs as examples were successfully synthesized, and as electrodes they exhibited superior supercapacitive performance with excellent long-term cycle stability and high energy and power densities.

Results

The proposed synthetic pathway to single-walled nanotubes is illustrated in Figure 1a. In this study, ZnO nanorod arrays (NRAs) attached on conductive substrate are firstly synthesized and utilized as templates, and then the electropolymerization of polypyrrole (PPy) is carried out on the surfaces of ZnO NRAs to form ZnO/PPy core-shell NRAs. Finally, PPy NTAs are fabricated by etching ZnO from ZnO/PPy core-shell NRAs. This method shows following advantages: the wall thickness of PPy nanotubes can be well controlled by adjusting electro-polymerization time as shown in Figure 1b, and the outside and inside diameters of nanotubes can be well
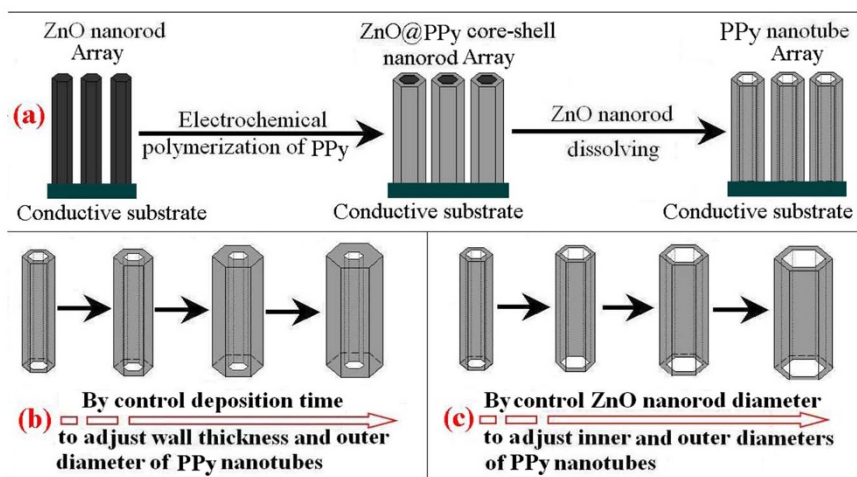
Figure 1 | (a) Illustration of formation of PPy nanotube arrays via ZnO nanorod template route; (b) the control of diameter of PPy nanotubes; (c) the control of wall thickness of PPy nanotubes.

controlled by adjusting the wall thickness and diameters of ZnO nanorod precursors as shown in Figures 1b and 1c.

The details of experimental procedures are described in Methods. SEM image of the prepared ZnO NRAs is shown in Figure 2a. The electropolymerization of PPy on the surfaces of ZnO NRAs was studied in supporting information (SI). ZnO@PPy core-shell NRAs were synthesized by electro-deposition of PPy on the surfaces of ZnO NRAs, and their SEM image is shown in Figure 2b, which shows ZnO nanorods have uniform PPy wraps. Furthermore, the PPy wraps favorably share the surfaces of ZnO NRAs, and no PPy is packed into the interspaces of ZnO nanorods, which suggests PPy is preferentially deposited on the surfaces of ZnO nanorods. The diameters of ZnO@PPy core-shell nanorods are ∼500 nm, and the thicknesses of PPy layers are ∼120 nm. PPy NTAs are fabricated by etching ZnO from ZnO@PPy core-shell NRAs in ammonia solution, and their SEM image is shown in Figure 2c. The outside and inside diameters of PPy nanotubes are ∼500 and ∼280 nm, respectively. TEM image of PPy nanotube is shown in Figure 2d, which further indicates the formation of PPy nanotubes. Herein, the inside

diameter of PPy nanotube is well tunable by adjusting the size of ZnO nanorod template. SEM images of various PPy nanotubes with inside diameters of 200, 250, 300, and 400 nm are shown in Figure 3. The wall thickness of PPy nanotube also can be well controlled by changing the electropolymerization time as shown in Figure S3. When the electropolymerization time is 5, 15 30, and 45 min, the wall thicknesses of PPy nanotubes are about 19, 34, 69, and 120 nm, respectively. In addition, the lengths of PPy nanotubes is well tunable by adjusting the lengths of ZnO nanorods. The lengths of various PPy nanotubes shown in Figures S4a, S4b, S4c, and S4d are about 500 nm, 1.0 μm, 1.5 μm, and 2.0 μm, respectively. PPy NTAs were also characterized by XRD, FT-IR, Raman, and UV spectra, and these results demonstrated the successful synthesis of PPy NTAs as shown in SI.

MnO_2 has been considered to be one of the most attractive electrode materials for supercapacitors owing to its high theoretical specific capacitance, low cost, natural abundance, and environmental friendliness[42,43]. Here MnO_2/PPy/MnO_2 triple-walled nanotube arrays (TNTAs) is also designed and fabricated via the ZnO nanorods-assisted electrodeposition route, and the procedure is shown in Figure 4. Firstly, ZnO NRAs attached on conductive substrate are prepared and utilized as templates. Secondly, the electrodeposition of
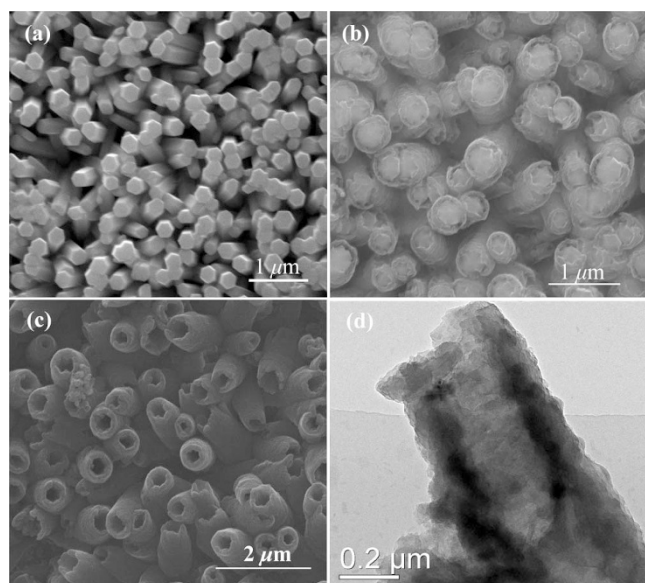

Figure 2 | SEM images of (a) ZnO NRAs, (b) ZnO@PPy core-shell NRAs, and (c) PPy NTAs after etching ZnO nanorods. (d) TEM image of a typical PPy nanotube.
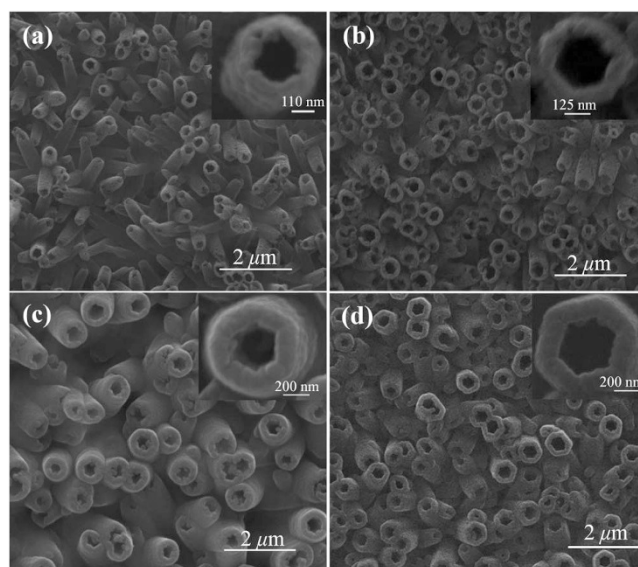

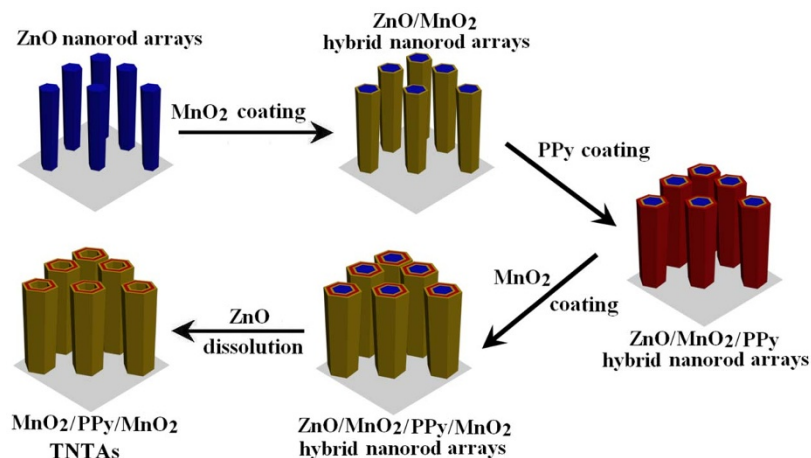**Figure 3** | SEM images of PPy nanotube arrays with different diameters.

Figure 4 | Schematic illustration for synthesis of MnO₂/PPy/MnO₂ TNTAs.

MnO$_2$ is carried out on the surfaces of ZnO nanorods to form ZnO/MnO$_2$ hybrid NRAs. Thirdly, the electropolymerization of PPy is carried out on the surf-aces of ZnO/MnO$_2$ NRAs to form ZnO/MnO$_2$/PPy NRAs. Fourthly, MnO$_2$ is further electrodeposited on the surfaces of ZnO/MnO$_2$/PPy NRAs to form ZnO/MnO$_2$/PPy/MnO$_2$ NRAs. Finally, MnO$_2$/PPy/MnO$_2$ TNTAs are facilely synthesized by dissolving ZnO from ZnO/MnO$_2$/PPy/MnO$_2$ NRAs in a weak basic solution. The details of fabrication are described in the experimental section. SEM images of ZnO NRAs, ZnO/MnO$_2$ NRAs, ZnO/MnO$_2$/PPy NRAs, ZnO/MnO$_2$/
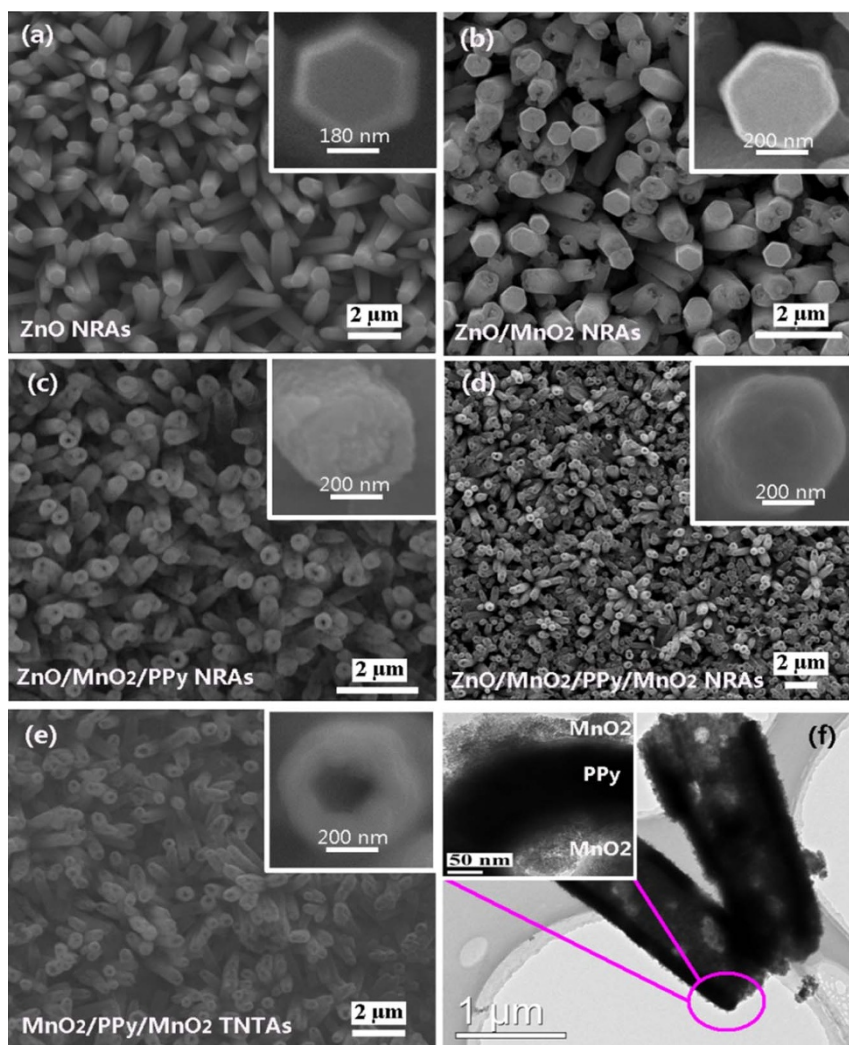

Figure 5 | SEM images of (a) ZnO NRAs, (b) ZnO/MnO₂ NRAs, (c) ZnO/MnO₂/PPy NRAs, (d) ZnO/MnO₂/PPy/ MnO₂ NRAs, and (e) MnO₂/PPy/ MnO₂ TNTAs. (f) TEM image of MnO₂/PPy/MnO₂ TNTAs.
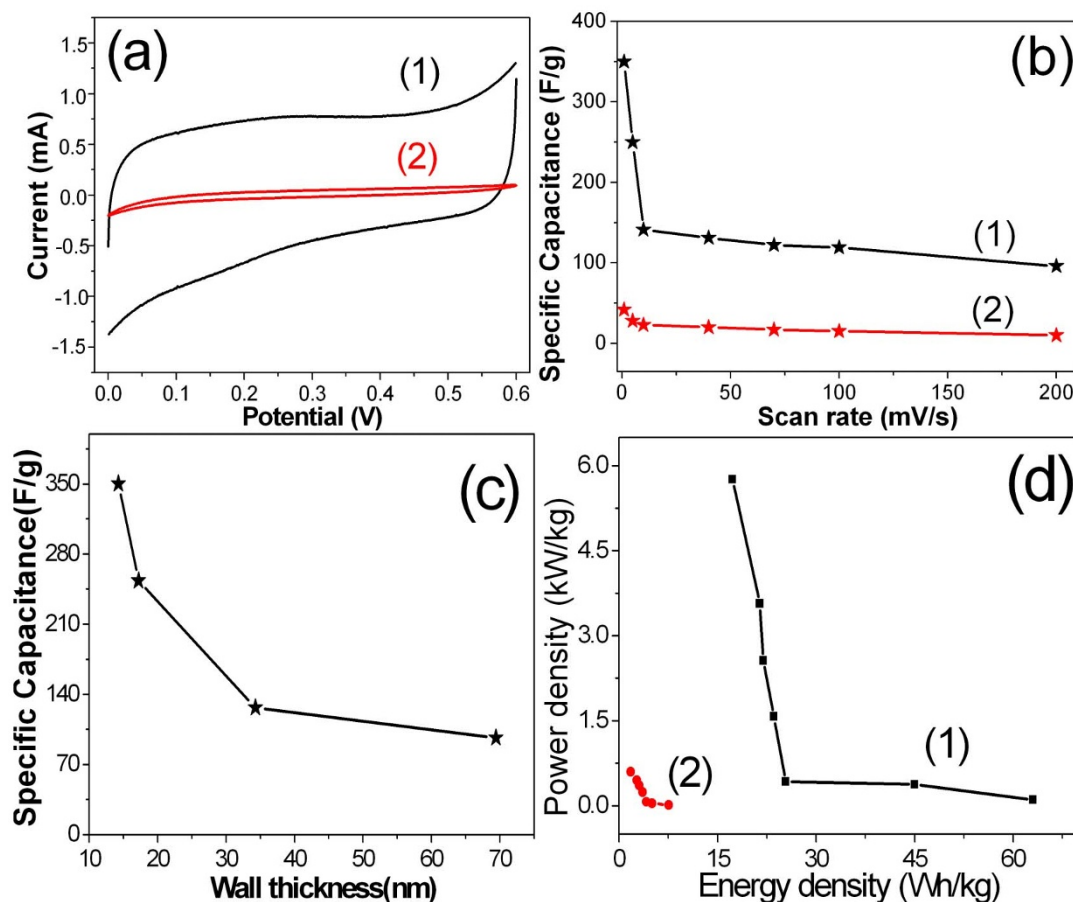
Figure 6 | (a) CVs of (1) PPy NTAs and (2) bulk films at scan rate of 1.0 mV/s; (b) C_{sp} of (1) PPy NTAs and (2) bulk films as a function of scan rate; (c) C_{sp} of PPy NTAs as a function of wall thickness; (d) Ragone plot (power density *vs* energy density) of (1) PPy NTAs and (2) bulk films.

PPy/MnO$_2$ NRAs, and MnO$_2$/PPy/MnO$_2$ TNTAs are shown in Figures 5a, 5b, 5c, 5d and 5e, respectively. It is clearly observed that the MnO$_2$/PPy/MnO$_2$ TNTAs have smooth surfaces and lengths of about 2 μm and separate from each other. Their diameters and wall thicknesses are about 700 nm and 250 nm, respectively. The highly void volume is clearly observed in MnO$_2$/PPy/MnO$_2$ TNTAs, and it will provide a three-dimensional (3D) space for the mass transfer of reactant and resultant molecules or ions. A typical transmission electron microscopy (TEM) image in Figure 5f further demonstrate the MnO$_2$/PPy/MnO$_2$ TNTAs were successfully fabricated, and they have homogeneous wall thickness of about 250 nm. The thicknesses of inner MnO$_2$ layer, middle PPy layer, and outer MnO$_2$ layer in nanotube walls are 65, 125, 60 nm, respectively. The inner and outer MnO$_2$ layers both are porous structures as shown in inset in Figure 5f, which will provide a large surface area and fast ion diffusion.

XPS spectra of MnO$_2$/PPy/MnO$_2$ TNTAs in the energy regions of Mn2p and O1s are shown in Figures S6(a) and S6(b), respectively. In Figure S6(a), the detected two peaks at the binding energies of 641.9 eV and 653.1 eV can be attributed to Mn 2p$_{3/2}$ and Mn 2p$_{1/2}$, respectively, indicating that the element Mn in the sample is present in the chemical state of Mn(IV)[37]. The O1s spectrum in Figure S6(b) demonstrates the existence of O. So the above XPS results demonstrate that the MnO$_2$ exists in the products. FT-IR spectrum of MnO$_2$/PPy/MnO$_2$ TNTAs is shown in Figure S7, and it demonstrates the existence of PPy in the products. XRD pattern of the prepared MnO$_2$/PPy/MnO$_2$ TNTAs is shown in Figure S8. The peak of PPy is not seen in XRD, indicating PPy is amorphous. The peaks of MnO$_2$ are clearly observed in XRD, indicating MnO$_2$ in MnO$_2$/PPy/MnO$_2$ TNTAs is crystalline. HRTEM and SAED results

further exihibit MnO$_2$ layers are polycrystalline as shown in Figure S9. The impedance curves of MnO$_2$/PPy/MnO$_2$ TNTAs and MnO$_2$ NTAs in solution of 1.0 M LiOH are shown in Figure S10, which shows MnO$_2$/PPy/MnO$_2$ TNTAs have higher conductivity than MnO$_2$ NTAs, demonstrating the role of middle PPy layers for conductivity enhancement of electrodes.

Discussion

The supercapacitive performances of PPy NTAs were studied by means of cyclic voltammetry (CV). Figure 6a(1) shows CV curve of PPy NTAs in 1.0 M H$_2$SO$_4$ solution at 1.0 mV/s. The nearly rectangular shape is exhibited in CV curve, indicating the symmetric current-potential characterisics and good supercapacitive properties. The specific capacitance (Csp) of PPy NTAs is calculated to be about 350 F/g at 1.0 mV/s. For PPy bulk film electrode, the C_{sp} is calculated to be only about 42 F/g at the same scan rate, which is much smaller than that of PPy NTAs. The high C_{sp} of PPy NTAs can be attributed to the large surface area and special nanotube array structures. The dependence of C_{sp} on scan rate is shown in Figure 6b, which shows C_{sp} of PPy is much larger than bulk PPy film at all scan rates. The C_{sp} *vs*. wall thickness of PPy NTAs is shown in Figure 6c, and the length effect of PPy nanotubes on capacitive performances is shown in Figure S11. Figure 6d shows Ragone plots (power density *vs* energy density) of PPy NTAs and bulk films. The PPy NTAs delivered a high energy density of ~17 Wh/kg at a power density of ~5.8 kW/kg, much superior to PPy bulk films.

To compare with PPy NTAs, the supercapacitive properties of MnO$_2$/PPy/MnO$_2$ TNTAs is also studied. Figure 7a shows cyclic voltammograms (CVs) of MnO$_2$/PPy/MnO$_2$ TNTAs with potential window ranging from −0.3 to 0.3 V *vs* SCE at different scan rates,
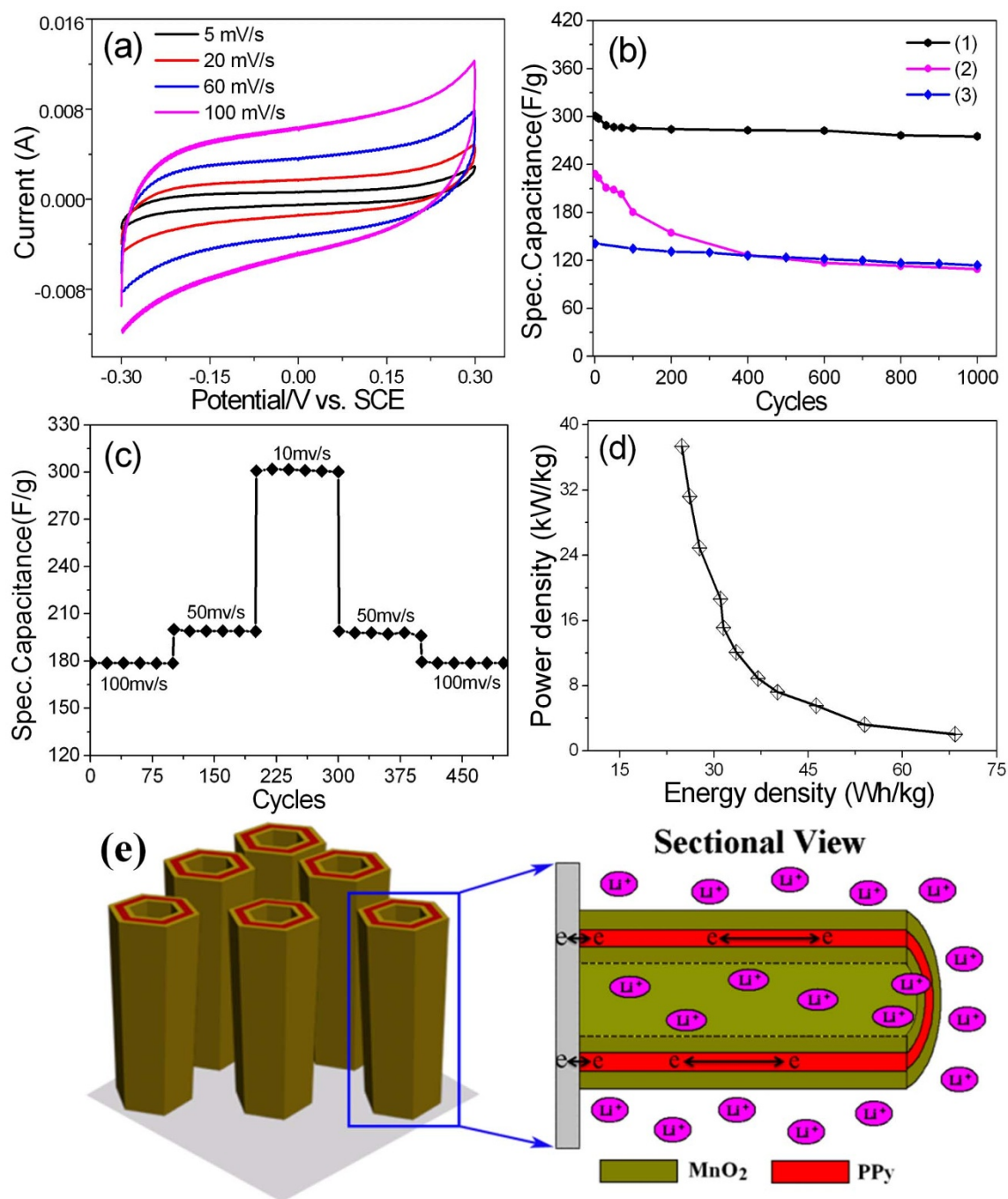
Figure 7 | (a) CVs of MnO$_2$/PPy/MnO$_2$ TNTAs at different scan rates; (b) C_{sp} of (1) MnO$_2$/PPy/MnO$_2$ TNTAs, (2) MnO$_2$ NTAs, and (3) PPy NTAs as a function of cycle number at 10 mV/s; (c) Cycling stability at progressively varied scan rates; (d) Ragone plot (power density *vs* energy density) of MnO$_2$/PPy/MnO$_2$ TNTAs; (e) The NTA architectures, triple layered structures, and high conductivity in electrodes provide ion and electron "highways" for extremely rapid charge/discharge processes.

and the quasi-rectangular shapes are exhibited in all CV curves, indicating the symmetric current-potential characteristics and well supercapacitive properties. The C_{sp} of MnO$_2$/PPy/MnO$_2$ TNTAs at 5 mV/s is calculated about 379 F/g, which is larger than 277 F/g of MnO$_2$ NTAs and 250 F/g of PPy NTAs at the same scan rate, and is also larger than some C_{sp} values reported for MnO$_2$ and PPy samples[44–46]. The enhancement of C_{sp} of MnO$_2$/PPy/MnO$_2$ TNTAs can be attributed to the co-contributions of supercapacitive PPy and MnO$_2$, ordered NTAs architecture, high conductivity of PPy layers, and porous double-layered MnO$_2$ layers. The dependence of C_{sp} on scan rate is shown in Figure S12, which shows a C_{sp} decay of ~37%

for MnO$_2$/PPy/MnO$_2$ TNTAs with scan rate increasing from 5 to 250 mV/s. Even at a scan rate as high as 250 mV/s, the C_{sp} of MnO$_2$/PPy/MnO$_2$ TNTAs still achieve a high value as large as 238 F/g. However, MnO$_2$ NTAs show a C_{sp} decay of 64% and 99 F/g at 250 mV/s. PPy NTAs show a C_{sp} decay of 65% and 89 F/g at 250 mV/s. The above results indicate MnO$_2$/PPy/MnO$_2$ TNTAs have a much better rate capability and much larger C_{sp} than MnO$_2$ NTAs and PPy NTAs at all scan rates as shown in Figure S12.

Excellent cycling stability is crucial for electrochemical capacitor (EC) operations. The C_{sp} variation of MnO$_2$/PPy/MnO$_2$ TNTAs as a function of cycle number at a scan rate of 10 mV/s is shown in

Figure 7b, which shows a small decrease of about 7.8% in C_{sp} up to 1000 cycles. As revealed from the above data, the $MnO_2/PPy/MnO_2$ TNTAs almost can withstand over 1000 cycles at 10 mV/s without any significant decrease in C_{sp}. In addition, the electrolyte solution still remains transparent after the cycling test, indicating almost no dissolution of electrode material into the solution. The PPy NTAs show a C_{sp} decay of about 18.6% after 1000 cycles, which is more serious than that of $MnO_2/PPy/MnO_2$ TNTAs. However, for MnO_2 NTAs, the C_{sp} decay is about 52.8% after 1000 cycles, which is much more serious than that of $MnO_2/PPy/MnO_2$ TNTAs and PPy NTAs. Therefore, the above results demonstrate that the $MnO_2/PPy/MnO_2$ TNTAs, as active electrode materials, are much higher stability than PPy NTAs and MnO_2 NTAs during long-term cycling test. The combination of MnO_2 and PPy into a unique TNTA morphology not only enhance C_{sp} but also improve the long-term stability compared with MnO_2 nanotube arrays and PPy nanotube arrays.

The high C_{sp} and excellent long-term cycle stability show such design of $MnO_2/PPy/MnO_2$ TNTAs allow to maximize the electrochemical performances of electrode. The $MnO_2/PPy/MnO_2$ TNTAs show following advantages as EC electrodes: (i) the 3D TNTAs with the anisotropic morphology, large surface area and hollow nanostructures create efficient diffusion paths for electrolyte ions, which would significantly accelerate intercalation of ions and, accordingly, enhance utilization rate of electrode materials as shown in Figure 7e. (ii) the conductive networks in electrode are well-built since the MnO_2 shells are attached tightly on PPy layers that have high electrical conductivity and the TNTAs have an excellent electrical contact with the current collector, and accordingly the utilization rate of electrode material is largely enhanced by decreasing the ohmic resistivity of electrode because of the existence of polarization. (iii) the combination of MnO_2 and PPy into a single engineered nanoarchitecture and the synergistic effects from MnO_2 and PPy largely contribute to the enhancement of pesudocapacitive performances of electrode. In addition, the composites of PPy and MnO_2 have excellent complementarity compared with individual PPy and MnO_2 and the following advantages have been demonstrated: (a) the $MnO_2/PPy/MnO_2$ TNTAs show excellent long-term cycle stability and overcome the weak point of MnO_2 NTAs with poor cycle stability. As PPy NTAs and $MnO_2/PPy/MnO_2$ TNTAs both have much higher long-term cycle sbability than MnO_2 NTAs as shown in Figure 7b, so the PPy layers in $MnO_2/PPy/MnO_2$ TNTAs can be considered as the skeleton layers with high stability to maintain the structural integrity of TNTAs during long-term cycles. After 1000 cycles, the surface morphology of $MnO_2/PPy/MnO_2$ TNTAs is still kept well as shown in Figure S13. (b) the combination of PPy and MnO_2 leads to $MnO_2/PPy/MnO_2$ TNTAs have much higher C_{sp} than the individual PPy and MnO_2 NTAs because of their co-contributions to C_{sp} as shown in Figure 7b. Based on the above analyse, therefore, the integrated smart TNTA architectures combining with the synergistic effects of PPy and MnO_2 promote the $MnO_2/PPy/MnO_2$ TNTAs to have high C_{sp} and excellent long-term cycle stability.

Herein, the advantages of $MnO_2/PPy/MnO_2$ TNTAs as electrodes for ECs were further investigated. The cycling performance of $MnO_2/PPy/MnO_2$ TNTAs at progressively increased and decreased scan rates were recorded, and they are shown in Figure 7c. After the electrode material suffered from sudden scan rate change, the fabricated $MnO_2/PPy/MnO_2$ TNTAs still show high cycle stabilities at various scan rates. The above results further demonstrate that the fabricated $MnO_2/PPy/MnO_2$ TNTAs can satisfy the requirements of both long-term cycle lifetime and good rate capability, which are highly important for use in the practical energy storage devices. In addition, the energy and power densities are important parameters for the investigation of electrochemical performance of the electrochemical cells. Herein, the Ragone plot (power density vs energy density) of $MnO_2/PPy/MnO_2$ TNTAs at various scan rates is shown in Figure 7d, which shows the $MnO_2/PPy/MnO_2$ TNTAs deliver a high energy density of ~25 Wh/kg at a high power density of ~37 kW/kg. The power density of $MnO_2/PPy/MnO_2$ TNTAs ranges from 2.0 to 37.4 kW/kg, and the energy density ranges from 25 to 68 Wh/kg with scan rate changing from 5 to 250 mV/s. These values are much higher than those of the conventional ECs[39]. Here the highest power density, 37.4 kW/kg, can adequately meet power demands of the PNGV (Partnership for a New Generation of Vehicles), 15 kW/kg, demonstrating the excellent capability of $MnO_2/PPy/MnO_2$ TNTAs for ECs as power supply components in hybrid vehicle systems. The above results suggest the $MnO_2/PPy/MnO_2$ TNTAs are a promising electrode material for ECs.

In summary, a novel ZnO nanorod template-assisted electrodeposition route for the synthesis of single- and multi-walled NTAs with controllable structures was reported. The inside and outside diameters, wall thicknesses, and lengths of nanotubes can be well controlled. The fabricated multi-walled NTAs allow high efficient utilization of electrode materials for electrochemical energy storage with facilitated transports of ions and electrons, and they showed predominant electrochemical performance, such as high C_{sp}, excellent long-term cycle stability, and high energy and power densities. The multi-walled nanostructures, orderly pore passages, hollow nanostructures, together with synergistic effects of different pesudocapacitive materials are mainly responsible for prominently enhanced electrochemical performance of multi-walled NTAs. The reported design concepts of electrode materials also can be utilized to other inorganic/organic hybrid materials, such as NiO, Co_3O_4, V_2O_5, and polyaniline, to build the multifunctional hybrid nano-/microstructures, which will be promising for a large spectrum of device applications.

Methods

Electrodeposition of ZnO nanorod precursors was performed with a HDV-7C transistor potentiostatic apparatus that connected with a simple three-electrode cell. Electrodeposition of PPy was performed with a DJS-209B potentiostatic apparatus connected with a simple three electrode cell. The graphite electrode was used as a counter electrode (spectral grade, 1.8 cm²). The saturated calomel electrode (SCE) was used as the reference electrode that was connected to the cell with a double salt bridge system. The Ti plates (99.99 wt%, 1.5 cm²) were used as the substrate for electropolymerization, and they are prepared complying the following steps before each experiment: firstly polished by SiC abrasive paper from 300 to 800 grits, then dipped in HCl solution (5%) for 5 min and rinsed with acetone in ultrasonic bath for 5 min, and finally washed by distilled water.

Fabrication of PPy nanotube arrays (NTAs). ZnO nanorod arrays (NRAs) were electrodeposited in solution of 0.01 M $Zn(NO_3)_2$ + 0.05 M NH_4NO_3 by galvanostatic electrolysis with 1.0 mA/cm² for 90 min at 70°C. Then the electropolymerization of PPy was further carried out on the surfaces of ZnO NRAs in solution of 0.1 M pyrrole + 0.05 M Na_2SO_4 at 70°C by galvanostatic electrolysis with current density of 2 mA/cm² for 30 min, and accordingly ZnO/PPy core-shell NRAs were obtained. Finally, PPy NTAs were obtained by dissolving ZnO from ZnO/PPy core-shell NRAs in ammonia solution (25%).

Fabrication of $MnO_2/PPy/MnO_2$ triple-walled nanotube arrays (TNTAs). After the fabrication of ZnO NRAs, MnO_2 layers were then electrodeposited on the surfaces of ZnO NRAs in aqueous solution of 0.01 M $Mn(NO_3)_2$ + 0.02 M NH_4NO_3 + 10% dimethyl sulfoxide (DMSO) by galvanostatic electrolysis at 0.1 mA·cm⁻² for 30 min at 70°C using HDV-7C transistor potentiostatic apparatus, and accordingly ZnO/MnO_2 hybrid NRAs were obtained. PPy layers were further electrodeposited on the surfaces of ZnO/MnO_2 NRAs in a solution of 0.01 M pyrrole + 0.05 M Na_2SO_4 by galvanostatic electrolysis at 1.0 mA·cm⁻² for 30 min at 70°C using DJS-292B transistor potentiostatic apparatus, and ZnO/MnO_2/PPy hybrid NRAs were fabricaced. After that, MnO_2 layer was further electrodeposited on the surfaces of ZnO/MnO_2/PPy hybrid NRAs in aqueous solution of 0.01 M $Mn(NO_3)_2$ + 0.02 M NH_4NO_3 + 10% DMSO at 0.1 mA/cm² for 30 min at 70°C using HDV-7C transistor potentiostatic apparatus, and the ZnO/MnO_2/PPy/MnO_2 four-layered hybrid NRAs were obtained. Finally, the ZnO/MnO_2/PPy/MnO_2 four-layered hybrid NRAs were put into 25% ammonia water for 2 h to remove ZnO NRAs, and accordingly the inorganic/organic hybrid MnO2/PPy/MnO2 TNTAs were successfully fabricated.

Characterization of samples. The surface morphologies and structures of the fabricated samples were examined by using field emission environment scanning electron microscope (SEM, Quanta 400) and transmission electron microscopy (TEM, JEOL JEM-2010HR; accelerating voltage: 200 kV). The fabricated samples were also characterized by energy-dispersive X-ray spectroscopy (EDS, INCA 300) to

determine the deposit compositions. The structures of fabricated samples were analyzed by X-ray diffraction (XRD, PIGAKU, D/MAX 2200 VPC). Chemical-state analysis of samples was carried out by X-ray photoelectron spectroscopy (XPS) using an ESCALAB 250 X-ray photo-electron spectrometer. All XPS spectra were corrected using the C 1s line at 284.6 eV. Curve fitting and background subtraction were accomplished. The samples were also characterized by infrared ray spectrometer (FT-IR, Nicolet 330). Raman scattering spectra were recorded with a Renishaw System 2000 spectrometer using the 514 nm line of Ar for excitation. The electrochemical properties of PPy NTAs (1.71 mg) and MnO_2/PPy/MnO_2 TNTAs (0.31 mg) were studied by a CHI760D electrochemical workstation by cyclic voltammetry at room temperature. The cyclic voltammetry experiments were performed at a scan rate of 1~250 mV/s.

1. Cho, S. & Lee, S. B. Fast electrochemistry of conductive polymer nanotubes: synthesis, mechanism, and application. *Account. Chem. Res.* **41**, 699–707 (2008).
2. Abidian, M. R., Kim, D.-H. & Martin, D. C. Conducting-polymer nanotubes for controlled drug release. *Adv. Mater.* **18**, 405–409 (2006).
3. Xiao, R., Cho, S. I., Liu, R. & Lee, S. B. Controlled electrochemical synthesis of conductive polymer nanotube structures. *J. Am. Chem. Soc.* **129**, 4483–4489 (2007).
4. Kwon, O. S., Park, S. J., Lee, J. S., Park, E., Kim, T., Park, H.-W., You, S. A., Yoon, H. & Jang, J. Multidim-ensional conducting polymer nanotubes for ultrasensitive chemical nerve agent sensing. *Nano Lett.* **12**, 2797–2802 (2012).
5. Ren, J., Li, L., Chen, C., Chen, X., Cai, Z., Qiu, L., Wang, Y., Zhu, X. & Peng, H. Twisting carbon nanotube fibers for both wire-shaped micro-supercapacitor and micro-battery. *Adv. Mater.* **24**, DOI: 10.1002/adma.201203445 (2012).
6. Dickey, M. D., Weiss, E. A., Smythe, E. J., Chiechi, R. C., Capasso, F. & Whitesides, G. M. Fabrication of arrays of metal and metal oxide nanotubes by shadow evaporation. *ACS Nano* **2**, 800–808 (2008).
7. Xiao, F. Layer-by-layer self-assembly construction of highly ordered metal-TiO_2 nanotube arrays heterostructures (M/TNTs, M=Au, Ag, Pt) with tunable catalytic activities. *J. Phys. Chem. C* **116**, 16487–16498 (2012).
8. Liu, P., Zhang, H., Liu, H., Wang, Y., Yao, X., Zhu, G., Zhang, S. & Zhao, H. A facile vapor-phase hydrothermal method for direct growth of titanate nanotubes on a titanium substrate via a distinctive nanosheet roll-up mechanism. *J. Am. Chem. Soc.* **133**, 19032–19035 (2011).
9. Hu, S. & Wang, X. Single-walled MoO_3 nanotubes. *J. Am. Chem. Soc.* **130**, 8126–8127 (2008).
10. Ye, M., Xin, X., Lin, C. & Lin, Z. High efficiency dye-sensitized solar cells based on hierarchically structured nanotubes. *Nano Lett.* **11**, 3214–3220 (2011).
11. So, S., Lee, K. & Schmuki, P. Hepatocyte-targeting single galactose-appended naphthalimide: a tool for intracellular thiol imaging in vivo. *J. Am. Chem. Soc.* **134**, 1316–1322 (2012).
12. Roy, P., Das, C., Lee, K., Hahn, R., Ruff, T., Moll, M. & Schmuki, P. Oxide nanotubes on Ti−Ru alloys: strongly enhanced and stable photoelectrochemical activity for water splitting. *J. Am. Chem. Soc.* **133**, 5629–5631 (2011).
13. Huang, X., Wang, M., Willinger, M.-G., Shao, L., Su, D. S. & Meng, X.-M. Assembly of three-dimensional heteroepitaxial ZnO/ZnS core/shell nanorod and single crystalline hollow ZnS nanotube arrays. *ACS Nano* **6**, 7333–7339 (2012).
14. Li, Q., Wang, Z., Li, G., Guo, R., Ding, L. & Tong, Y. Design and synthesis of MnO_2/Mn/MnO_2 sandwich-structured nanotube arrays with high supercapacitive performance for electrochemical energy-storage. *Nano Lett.* **12**, 3803–3807 (2012).
15. Dahlberg, K. A. & Schwank, J. W. Synthesis of Ni@SiO_2 nanotube particles in a water-in-oil microemulsion template. *Chem. Mater.* **24**, 2635–2644 (2012).
16. Ding, L.-X., Wang, A.-L., Li, G.-R., Liu, Z.-Q., Zhao, W.-X., Su, C.-Y. & Tong, Y.-X. Porous Pt-Ni-P composite nanotube arrays: highly electroactive and durable catalysts for methanol electrooxidation. *J. Am. Chem. Soc.* **134**, 5730–5733 (2012).
17. Michell, R. M., Lorenzo, A. T., Müller, A. J., Lin, M.-C., Chen, H.-L., Blaszczyk-Lezak, I., Martín, J. & Mijangos, C. The crystallization of confined polymers and block copolymers In filtrated within alumina nanotube templates. *Macromolecules* **45**, 1517–1528 (2012).
18. Song, T., Cheng, H., Choi, H., Lee, J.-H., Han, H., Lee, D. H., Yoo, D. S., Kwon, M.-S., Choi, J.-M., Doo, S. G., Chang, H., Xiao, J., Huang, Y., Park, W. I., Chung, Y.-C., Kim, H., Rogers, J. A. & Paik, U. Si/Ge double-layered nanotube array as a lithium ion battery anode. *ACS Nano* **6**, 303–309 (2012).
19. Sun, B., Hao, Y., Guo, F., Cao, Y., Zhang, Y., Li, Y. & Xu, D. Fabrication of poly(3-hexylthiophene)/CdS/ ZnO core-shell nanotube array for semiconductor-sensitized solar cell. *J. Phys. Chem. C.* **116**, 1395–1412 (2012).
20. He, H., Cai, W., Lin, Y. & Dai, Z. Silver porous nanotube built three-dimensional films with structural tunability based on the nanofiber template-plasma etching strategy. *Langmuir* **27**, 1551–1555 (2011).
21. Zhang, J., Bang, J. H., Tang, C. & Kamat, P. V. Tailored TiO2-SrTiO3 heterostructure nanotube arrays for improved photoelectrochemical performance. *ACS Nano* **4**, 387–395 (2010).
22. Chen, Y.-Y., Yu, B.-Y., Wang, J., Cochran, R. E. & Shyue, J.-J. Template-based fabrication of SrTiO3 and BaTiO3 nanotubes. *Inorg. Chem.* **48**, 681–686 (2009).
23. Gao, Y., Li, X., Gong, J., Fan, B., Su, Z. & Qu, L. Polyaniline Nanotubes Prepared Using Fiber Mats Membrane as the Template and their Gas-response Behavior. *J. Phys. Chem. C* **112**, 8215–8222 (2008).
24. Zhou, M., Zhu, H., Wang, X., Xu, Y., Tao, Y., Hark, S., Xiao, X. & Li, Q. CdSe Nanotube Arrays on ITO via Aligned ZnO Nanorods Templating. *Chem. Mater.* **22**, 64–69 (2010).
25. Mitchell, D. T., Lee, S. B., Trofin, L., Li, N., Nevanen, T. K., Söderlund, H. & Martin, C. R. Smart nanotubes for bioseparations and biocatalysis. *J. Am. Chem. Soc.* **124**, 11864–11865 (2002).
26. Gao, C., Zhang, Q., Lu, Z. & Yin, Y. Templated synthesis of metal nanorods in silica nanotubes. *J. Am. Chem. Soc.* **133**, 19706–19709 (2011).
27. Son, S. J., Reichel, J., He, B., Schuchman, M. & Lee, S. B. Magnetic nanotubes for magnetic-field-assisted bioseparation, biointeraction, and drug delivery. *J. Am. Chem. Soc.* **127**, 7316–7317 (2005).
28. González-Rovira, L., Sánchez-Amaya, J. M., López-Haro, M., Rio, E., Hungría, A. B., Midgley, P., Calvino, J., Bernal, S. & Botana, F. J. Single-step process to prepare CeO_2 nanotubes with improved catalytic activity. *Nano Lett.* **9**, 1395–1400 (2009).
29. Ghicov, A., Aldabergenova, S., Tsuchiya, H. & Schmuki, P. TiO2-Nb2O5 nanotubes with electrochemically tunable morphologies. *Angew. Chem. Int. Edit.* **45**, 6993–6996 (2006).
30. Ai, S., Lu, G., He, Q. & Li, J. Highly flexible polyelectrolyte nanotubes. *J. Am. Chem. Soc.* **125**, 11140–1141 (2003).
31. Jayaraman, K., Okamoto, K., Son, S. J., Luckett, C., Gopalani, A. H., Lee, S. B. & English, D. S. Observing capillarity in hydrophobic silica nanotubes. *J. Am. Chem. Soc.* **127**, 17385–17392 (2005).
32. Hou, S., Wang, J. & Martin, C. R. Template-synthesized DNA nanotubes. *J. Am. Chem. Soc.* **127**, 8586–8587 (2005).
33. Wang, H.-J., Zhou, W.-H., Yin, X.-F., Zhuang, Z.-X., Yang, H.-H. & Wang, X.-R. Template synthesized molecularly imprinted polymer nanotube membranes for chemical separations. *J. Am. Chem. Soc.* **128**, 15954–15955 (2006).
34. Chen, C.-C., Liu, Y.-C., Wu, C.-H., Yeh, C.-C., Su, M.-T. & Wu, Y. C. Preparation of fluorescent silica nanotubes and their application in gene delivery. *Adv. Mater.* **17**, 404–407 (2005).
35. Lee, S. B., Mitchell, D. T., Trofin, L., Nevanen, T. K., Söderlund, H. & Martin, C. R. Antibody-based bio/ nanotube membranes for enantiomeric drug separations. *Science* **296**, 2198–2200 (2002).
36. Kohli, P., Harrell, C. C., Cao, Z., Gasparac, R., Tan, W. & Martin, C. R. DNA functionalized nanotube membranes with single-base mismatch selectivity. *Science* **305**, 984–986 (2004).
37. Siwy, Z., Trofin, L., Kohli, P., Baker, L. A., Trautmann, C. & Martin, C. R. Protein biosensors based on biofunctionalized conical gold nanotubes. *J. Am. Chem. Soc.* **127**, 5000–5001 (2005).
38. Hou, S., Harrell, C. C., Trofin, L., Kohli, P. & Martin, C. R. Layer-by-layer nanotube template synthesis. *J. Am. Chem. Soc.* **126**, 5674–5675 (2004).
39. Gu, D., Baumgart, H., Abdel-Fattah, T. M. & Namkoong, G. Synthesis of nested coaxial multiple-walled nanotubes by atomic layer deposition. *ACS Nano* **4**, 753–758 (2010).
40. Reddy, A. L. M., Shaijumon, M. M., Gowda, S. R. & Ajayan, P. M. Coaxial MnO_2/carbon nanotube array electrodes for high-performance lithium batteries. *Nano Lett.* **9**, 1002–1006 (2009).
41. Kim, M. J., Chatterjee, S., Kim, S. M., Stach, E. A., Bradley, M. G., Pender, M., Sneddon, L. & Maruyama, B. Double-walled boron nitride nanotubes grown by floating catalyst chemical vapor deposition. *Nano Lett.* **8**, 3298–3302 (2008).
42. Yu, G., Hu, L., Vosgueritchian, M., Wang, H., Xie, X., McDonough, J., Cui, X., Cui, Y. & Bao, Z. Solution-processed graphene/MnO_2 nanostructured textiles for high-performance electrochemical capacitors. *Nano Lett.* **11**, 2905–2911 (2011).
43. Wang, J., Yang, Y., Huang, Z.-H. & Kang, F. Rational synthesis of MnO_2/conducting polypyrrole@carbon nanofiber triaxial nanocables for high-performance supercapacitors. *J. Mater. Chem.* **22**, 16943–16949 (2012).
44. Li, J., Cui, L. & Zhang, X. Preparation and electrochemistry of one-dimensional nanostructured MnO_2/PPy composite for electrochemical capacitor. *Appl. Surf. Sci.* **256**, 4339–4343 (2010).
45. Jin, M., Han, G., Chang, Y., Zhao, H. & Zhang, H. Flexible electrodes based on polypyrrole/manganese dioxide/polypropylene fibrous membrane composite for supercapacitor. *Electrochimica Acta* **56**, 9838–9845 (2011).
46. Dong, Z. H., Wei, Y. L., Shi, W. & Zhang, G. A. Characterisation of doped polypyrrole/manganese oxide nanocomposite for supercapacitor electrodes. *Mater. Chem. Phys.* **131**, 529–534 (2011).

Acknowledgments

Author contributions

Z.-L.W. and R.G. planned and performed the experiments, collected and analyzed the data, and wrote the paper. G.-R.L. supervised the project, and conceived the experiments, analyzed the results and wrote the paper. L.X.D. and Y.-X.T. helped with synthesis of the

materials and collected the data. All authors discussed the results and commented on the manuscript.

Additional information